ARTICLE

Activatable Hyaluronic Acid Nanoparticle as a Theranostic Agent for Optical/Photoacoustic Image-Guided Photothermal Therapy

Liwen Zhang,[†] Shi Gao,[‡] Fan Zhang,[†] Kai Yang,[§] Qingjie Ma,[*,‡] and Lei Zhu[*,†]

[†]State Key Laboratory of Molecular Vaccinology and Molecular Diagnostics & Center for Molecular Imaging and Translational Medicine, School of Public Health, Xiamen University, Xiamen, Fujian, 361005, China, [‡]China-Japan Union Hospital, Jilin University, Changchun, Jilin 130033, China, and [§]School of Radiation Medicine and Protection & School for Radiological and Interdisciplinary Sciences (RAD-X), Collaborative Innovation Center of Suzhou Nano Science and Technology & Collaborative Innovation Center of Radiation Medicine of Jiangsu Higher Education Institutions, Medical College of Soochow University, Suzhou, Jiangsu 215123, China

ABSTRACT Photothermal therapy (PTT) is an emerging treatment modality that is under intensive preclinical investigations for the treatment of various medical conditions, including cancer. However, the lack of targeting function of PTT agents hampers its clinical application. An effective and nontoxic delivery vehicle that can carry PTT agents into tumor areas is still needed urgently. In this study, we developed a multifunctional nanocomposite by loading copper sulfide (CuS) into Cy5.5-conjugated hyaluronic acid nanoparticles (HANP), obtaining an activatable Cy5.5–HANP/CuS (HANPC) nanocomposite. In this system, Cy5.5 fluorescent signal is quenched by CuS inside the particle until the whole nanocomposite is degraded by hyaluronidase present in tumor, giving strong fluorescence signals delineating the tumor. Importantly, CuS with strong NIR absorbance appears to be an excellent contrast agent for photoacoustic (PA) imaging and an effective PTT agent. After intravenous administration of HANPC into SCC7 tumor-bearing mice, high fluorescence and PA signals were observed in the tumor area over time, which peaked at the 6 h time point (tumor-to-normal tissue ratio of 3.25 ± 0.25 for optical imaging and 3.8 ± 0.42 for PA imaging). The tumors were then irradiated with a laser, and a good tumor inhibition rate (89.74% on day 5) was observed. Our studies further encourage application of this HA-based multifunctional nanocomposite for image-guided PTT in biomedical applications, especially in cancer theranostics.

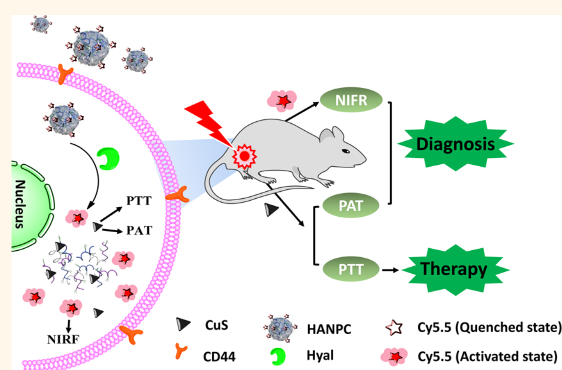

KEYWORDS: image-guided therapy · photothermal therapy · activatable probe · hyaluronic acid particles

To date, the development of multifunctional nanoplatforms that provide both diagnostic and therapeutic features has attracted great interests. Typically, nanoplatforms for theranostic purposes require biocompatibility, imaging, drug transport and targeting capabilities. An ideal multifunctional nanoplatform will provide: (i) early visualization of tumors or other disease sites, (ii) effective delivery of drugs into the site of interest, (iii) distribution of the theranostic agent *in vivo*, and (iv) optimized therapeutic strategy to reduce adverse side effects.[1−6] Among multifunctional nanoplatforms, activatable nanoparticles offer great benefits for theranostic applications. Similar to classic peptide-based activatable probes,[7−9] activatable theranostic nanoparticles keep an intact form before reaching the target, generally a molecular biomarker for dysfunction, such as overexpressed proteinase in a tumor.[10] Well-designed activatable theranostic nanoparticles are also able to selectively kill cancer cells by carrying a photosensitizer,[11] photothermal agent[12,13] or chemotherapeutic drug.[14] These types of activatable nanoparticles will not only make imaging-guided phototherapy possible, but also provide accurate disease detection and an optimized therapeutic strategy.

In recent decades, increasingly complicated efforts have been put to fabricate hyaluronic acid (HA) based nanoparticles.

* Address correspondence to lei.zhu@xmu.edu.cn, maqingjiejlu@163.com.

Received for review July 29, 2014 and accepted November 15, 2014.

Published online November 15, 2014
10.1021/nn506130t

© 2014 American Chemical Society

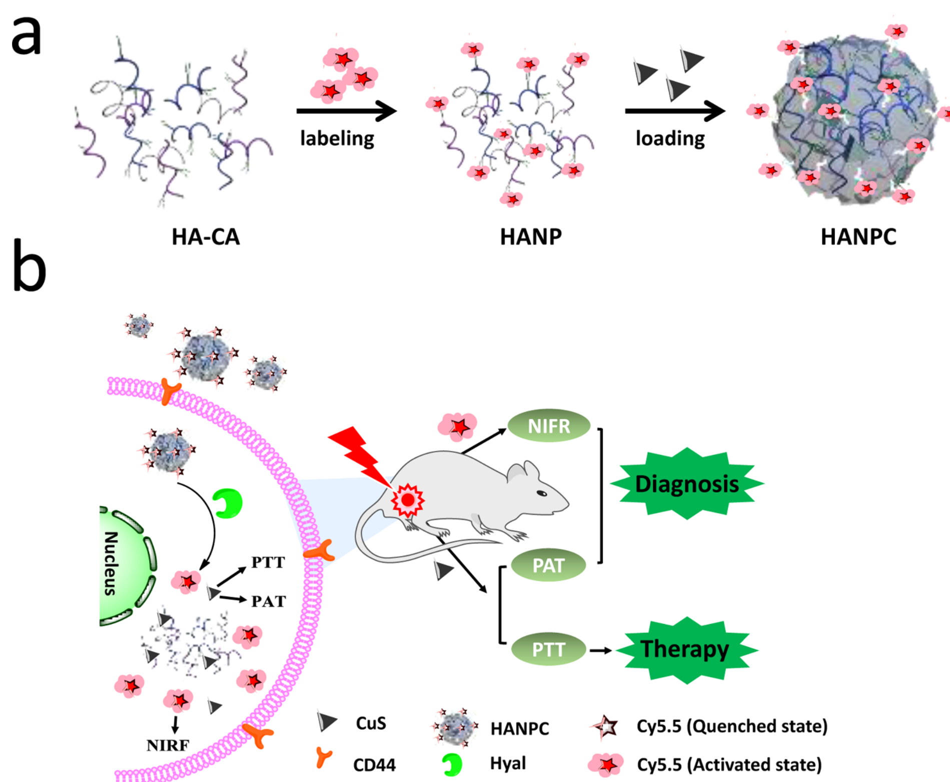

Scheme 1. Design and function of targeted nanocomplex. (a) Synthesis of targeted nanocomplex, HANPC. (b) *In vivo* applications of HANPC for NIR fluorescence and PA image-guided photothermal therapy.

HA, when chemically conjugated with a hydrophobic moiety like 5β-cholanic acid (5β-CA), can self-assemble into nanoparticles.[15−17] HA nanoparticles are an ideal carrier polymer for *in vivo* targeted delivery of imaging agents,[18] drugs,[3] and other biomedical materials. Compared with other nanoparticles, HA nanoparticles have greater cancer cell targeting efficiency *via* both passive and active targeting pathway. Specifically, when intravenously injected into tumor-bearing mouse model, HA nanoparticles accumulated in tumor effectively through the enhanced permeation and retention (EPR) effect and specifically bound to cancer cells those overexpressed cluster determinant 44 (CD44) or lymphatic vessel endothelial hyaluronan receptor-1 (LYVE-1).[19,20] Next, HANP will be internalized into tumor cells through receptor-mediated endocytosis, degraded into short saccharide units by hyaluronidases (mainly Hyal-1 and Hyal-2)[21,22] and released the cargo inside the cell. The active and passive targeting characteristics make HA nanoparticles ideal materials for *in vivo* applications, especially in cancer theranostics.

Photothermal therapy (PTT) is a modality that takes advantage of electromagnetic radiation to treat a variety of diseases, including cancer, without causing thermal injury to normal tissues.[23−28] Copper sulfide (CuS) nanoparticles are extensively investigated for PTT,[29−31] photoacoustic tomography (PAT),[32,33] drug delivery[34] and DNA detection,[35] due to the low cost, low cytotoxicity, and excellent optical and electrical properties.[36] However, CuS nanoparticles alone have limited applications in cancer diagnosis and therapy because of their poor tumor targeting property.[37]

To combine targeted PTT with fluorescence and photoacoustic (PA) imaging capabilities for treatment under NIR laser irradiation, we designed a multifunctional nanoparticle, which is a Cy5.5-conjugated HA nanoparticle loaded with CuS, and denoted as HANPC (Scheme 1). HANPC is hypothesized to accumulate in the tumor in a time dependent manner and provides structural PA imaging of biological tissues, such as the blood vessels in the tumor site. Meanwhile, the originally quenched HANPC will be degraded by hyaluronidases at the target site and is expected to boost strong optical signals, providing complementary information on PA from the whole body. Both PA and fluorescent imaging modalities are able to provide obvious tumor contrast in this study. At 6 h postinjection (p.i.), optical and PA signals reached peak intensity in the tumor, indicating a high tumor uptake of HANPC. Next, PTT was conducted on SCC7 tumor bearing mouse model, and therapeutic response was monitored for 2 weeks. Compared with control groups, effective ablation of SCC7 tumors was achieved *in vivo*. Our results greatly motivate the application of HANPC as a contrast agent for PA imaging and whole body optical imaging and simultaneously as therapeutic agents against tumors *in vivo*.

RESULTS AND DISCUSSION

Preparation and Characterization of HANPC. Hyaluronic acid (HA) nanoparticles (Supporting Information Figure S1) were synthesized as reported before[17] and labeled with a near-infrared dye, Cy5.5, for imaging purpose. The dye labeled HA nanoparticles was named as HANP. For photothermal therapy (PTT) with near-infrared laser irradiation, CuS was loaded into HANP by high pressure homogenizer. To optimize the ratio between CuS and HANP, different amounts of CuS (10%, 20%, and 40% w/w) were loaded into HANP and loading efficiency was calculated (Supporting Information Figure S2 and Table 1). We found that the highest loading efficiency was achieved when 20% CuS was applied. The mean particle size of HANP was 198.1 ± 11.5 nm and the size of HANPC was 227.2 ± 20.8 nm (Figure 1c) measured by transmission electron microscopy (TEM) and dynamic light scattering (DLS). There is about 30 nm size increase after CuS was loaded. Moreover, compared to HANP, HANPC demonstrated a remarkably higher absorption, which was contributed by CuS and was potentially favorable for PTT (Figure 1a). We also noticed that the fluorescent signals of Cy5.5 were nearly gone (Figure 1b) after CuS was loaded, indicating the high fluorescence quenching ability of CuS. To recover the fluorescence of HANPC, different amounts of hyaluronidase that degraded HA efficiently were added and incubated with HANPC. In these studies, fluorescent signals increased in a time-dependent manner. As shown in Figure 1b, the fluorescent signal increased 12.77-fold 2 h after adding hyaluronidase. The increase in fluorescent signal was also rely on the amount of hyaluronidase presents (Supporting Information Figure S4). These results suggest that HANPC, as an activatable nanoprobe, will efficiently respond to hyaluronidase that is overexpressed in the tumor area. Compared with free CuS, HANPC demonstrated excellent solubility and stability in water, PBS, FBS and cell medium (Figure 1d), supporting the idea that CuS is mostly loaded into the interior of the HANPs. Photoacoustics (PA) signals of HANPC were measured also as shown in Supporting Information Figure S6.

TABLE 1. CuS Loading Efficiency at Different Conditions

CuS to HANP ratio (wt %)	loading content (wt %)	yield (%)
1:9	7.86	78.6
1:4	17.47	87.35
2:3	20.07	50.18

Cell Internalization of HANP. After characterization, the HANP targeting ability was further investigated on both CD44 positive and negative cell lines by confocal microscopy. CD44 is a cell-surface receptor for HA and it is frequently overexpressed on the surface of tumor cells. After bound with CD44, HA will be internalized

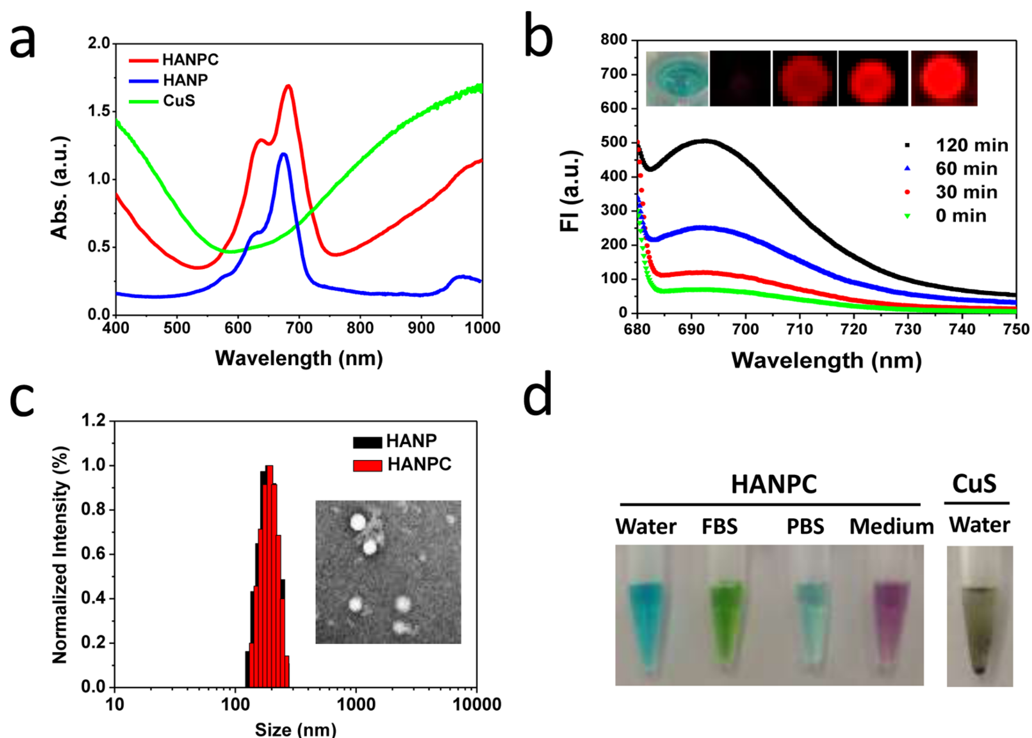

Figure 1. Characterization of HANPC. (a) UV/vis/NIR spectra of HANP, CuS and HANPC. (b) Fluorescence signal recovery of HANPC in the presence of hyaluronidase at indicated time points. Cy5.5 (ex/em: 670/690 nm) signals were monitored and recorded. A time-dependent increment was observed. Inset is fluorescent images of HANPC at different time points after degradation by hyaluronidase. (c) Particle size distribution of HANP and HANPC. Inset is TEM image of HANPC. (d) Stability of HANPC in water, PBS, fetal bovine serum (FBS), and cell medium. No precipitation was observed at 7 days after incubation. Free CuS was not dissolvable in water.

into the cells through a CD44 mediated pathway. As shown in Figure 2, strong fluorescence signals in CD44 positive SCC7 cells were observed, while little fluorescent signal was found in CD44 negative NIH3T3 cells. To investigate the binding specificity of HANP, we also performed a competitive binding study. CD44 receptors on SCC7 cells were first blocked by excess amount of free HA and treated with HANP. After 3 h incubation, much less fluorescent signal was observed in this study than SCC7 cells without CD44 blocking. These results suggested that HANP has a specific and strong binding ability with CD44 receptor and therefore can target the tumor area by both receptor mediated targeting and also the EPR effect. The dual-targeting property makes HANP a good candidate as an anticancer drug carrier.

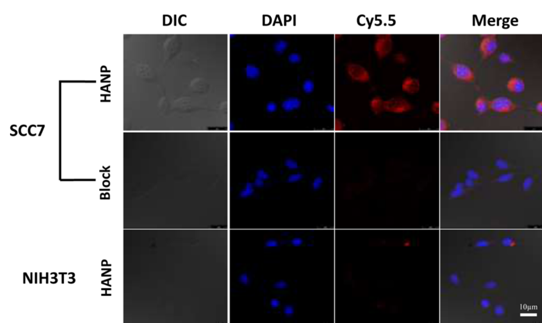

Figure 2. Cell internalization of HANP at different time points by SCC7 and NIH3T3 cells. HANP is effectively internalized by SCC7 cells *via* a CD44 mediated pathway. Due to the lack of CD44 expression, little HANP was internalized into NIH3T3 cells. The CD44 mediated cell internalization can be effectively inhibited by excess amount of free HA. The red color is from Cy5.5 (ex/em = 670/694 nm) on HANP representing its intracellular location and the blue color is from DAPI for nuclei staining. The scale bar is 20 μm.

***In Vitro* Photothermal Ablation Test of HNPC.** In view of the broad absorbance in the near-infrared region and high thermal capacity of CuS, CuS was loaded into HANP for tumor diagnosis and therapy. The final product was expected to provide the dual-targeting ability (CD44 binding and EPR effect), activatable optical imaging (quenching between Cy5.5 and CuS) function and PTT effect (CuS). First, the photothermal property of HANPC was checked under the irradiation of an 808 nm laser. HANPC (0.35 mg/mL) demonstrated a rapid temperature increase from 27 to 90 °C in 3 min (808 nm laser, 1 W/cm^2), suggesting a potential of HANPC in ablating cancer cells (Figure 3a,b and Supporting Information Figure S4). Furthermore, therapeutic activity of HANPC was evaluated *in vitro* by monitoring the viability of SCC7 cells after treatment with free CuS and HANPC with and without the presence of a laser (Figure 3c,d). HANPC showed significantly more suppression of SCC7

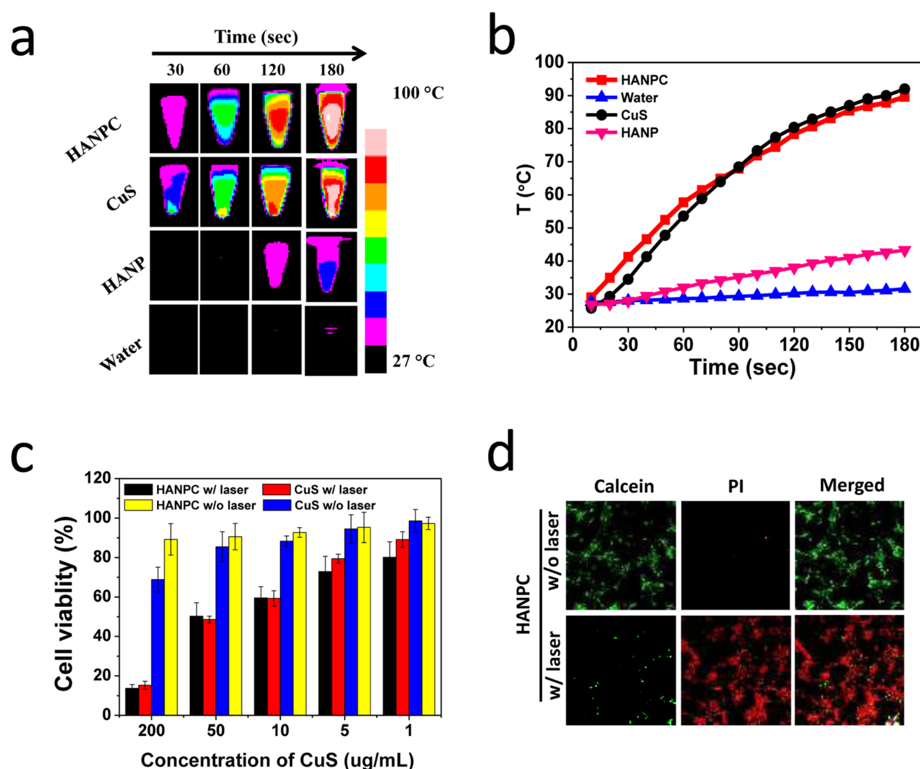

Figure 3. (a) *In vitro* photothermal ablation test. Real-time thermal imaging of HANPC, CuS, HANP, and water with laser irradiation (808 nm, 1 W/cm^2 for 3 min). (b) *In vitro* temperature change curve of HANPC, CuS, HANP, and water with laser irradiation (808 nm, 1 W/cm^2 for 3 min). (c). Cell viability studies with HANPC and free CuS with and without laser irradiation on SCC7 cells. Elevated cytotoxicity was found with increased amounts of HANPC in the presence of laser irradiation (808 nm, 1 W/cm^2 for 10 min). No significant cell death was found for both CuS and HANPC. (d) Calcein AM/PI staining to visualize SCC7 cell viability treated by HANPC with and without laser irradiation (808 nm, 0.5 W/cm^2 for 10 min). Green is propidium iodide (PI; ex/em = 535/615 nm) staining of dead cells and the red color is Calcein AM (ex/em = 490/515 nm) staining of live cells.

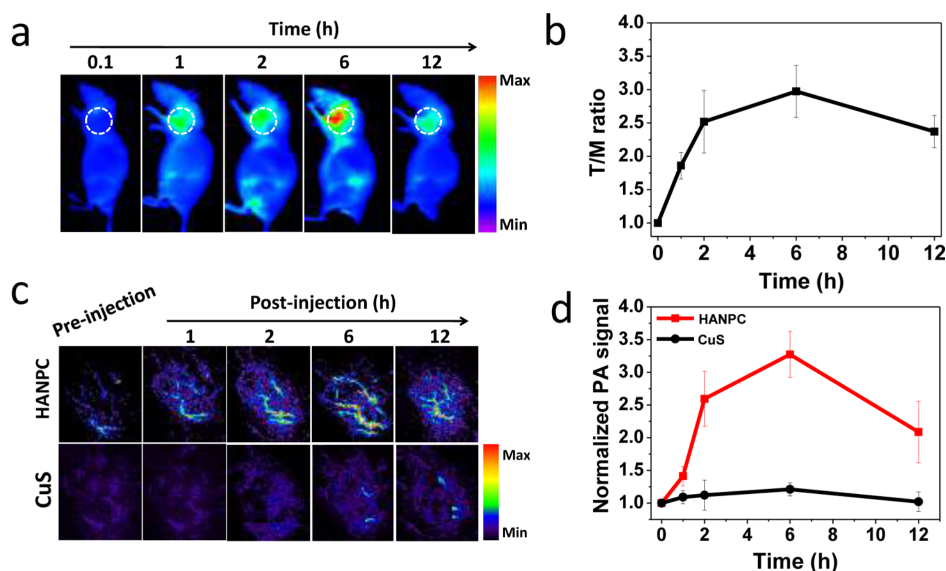

Figure 4. (a) NIR fluorescent imaging of CD44-positive SCC7 tumor-bearing mice received HANPC iv treatment. Images were acquired at indicated time points, and fluorescent signals were normalized by the maximum average value. The color bar indicates radiant efficiency (low, 0; high, 0.209×10^6). White circles were used to indicate tumors location. (b) Tumor/muscle (*T*/*M*) ratio of SCC7 tumor-bearing mouse model. Means $\pm$ SD ($n = 5$ per group). (c) Photoacoustic tomography imaging of blood vessels in SCC7 tumor-bearing mice intravenously received HANPC or free CuS. (d) Photoacoustic intensity of tumor tissues at different time points.

cell proliferation in a dose-dependent manner compared to those of HANP and free CuS under the same laser irradiation condition.

***In Vivo* Photoacoustic and Fluorescence Imaging of HANPC.** We then studied the *in vivo* biodistribution and tumor selectivity of HANPC in a subcutaneous (s.c.) SCC7 tumor model. HANPC (5 mg HANPC/kg) were intravenously (iv) administered, and fluorescence images were acquired at different time points postinjection. Excitation and emission wavelengths were set as 670/690 nm for Cy5.5. After injection, HANPC was degraded by hyaluronidase in the tumor area and the quenching effect between CuS and Cy5.5 was lessened, resulting in fluorescence signal recovery over time. Tumor-to-Muscle tissue (*T*/*M*) ratios were measured to be 1.86 $\pm$ 0.21, 2.52 $\pm$ 0.47, 2.94 $\pm$ 0.39, and 2.37 $\pm$ 0.24 at 1, 2, 6, and 12 h postinjection (p.i.), and suggesting good tumor targeting (Figure 4a,b=) by HANPC. Compared to NIR fluorescent imaging, photoacoustics (PA) imaging was a newly developed biomedical imaging modality with increased imaging depth and improved resolution that had attracted great interest recently. It was developed on the base of PA effect of certain materials with strong light absorbance. Although optical imaging allowed whole-body imaging, PA imaging is specifically helpful for analyzing the information in tumor area, for example tumor blood vessel distribution and the distribution of imaging agent. We applied PA imaging to observe the blood vessel distribution in the tumor area. As shown in Figure 4c,d, the PA contrast at the tumor site increased over time (1.41 $\pm$ 0.15, 2.59 $\pm$ 0.42, and 3.27 $\pm$ 0.35 at 1, 2, and 6 h p.i.) compared to that before injection. The PA contrast decreased to 2.09 $\pm$ 0.47 due to the clearance of CuS *in vivo* at 12 h post injection. Moreover, when free CuS without HANP was injected, only a slight increase of PA signal was observed due to the lack of targeting capability of CuS. *Ex vivo* imaging was performed as shown in Supporting Information Figure S5 by optical and PA imaging technic. In addition to accumulation in the SCC7 tumors, we found a high level of fluorescence activity and increased PA signals in the kidneys due to the degradation of HANPC. The uptake in other organs was much lower determined by both optical and PA imaging *ex vivo* (Supporting Information Figure S5). These results confirmed that the tumor specific accumulation of HANPC was mediated by the HANP. Our imaging results suggest that the 6 h time point is most appropriate for HANPC-mediated PTT because maximum accumulation of HANPC in the tumor area is achieved.

***In Vivo* Photothermal Therapy.** For photothermal treatment, SCC7 tumor mice were divided into eight groups randomly ($n = 5$/group): mice treated with PBS without laser irradiation, mice treated with PBS with laser irradiation, mice treated with HANP without laser irradiation, mice treated with HANP with laser irradiation, mice treated with CuS without laser irradiation, and mice treated with CuS with laser irradiation, mice treated with HANPC without laser irradiation, and mice treated with HANPC with laser irradiation. To verify the *in vivo* photothermal effect caused by CuS, we used an IR thermal camera to monitor the temperature increase in the tumor area. IR thermal graphic images indicated that in the HANPC group the tumor temperature rose rapidly to 42 °C in 1 min and continued to rise to about 50 °C at 4 min after laser irradiation. The laser power

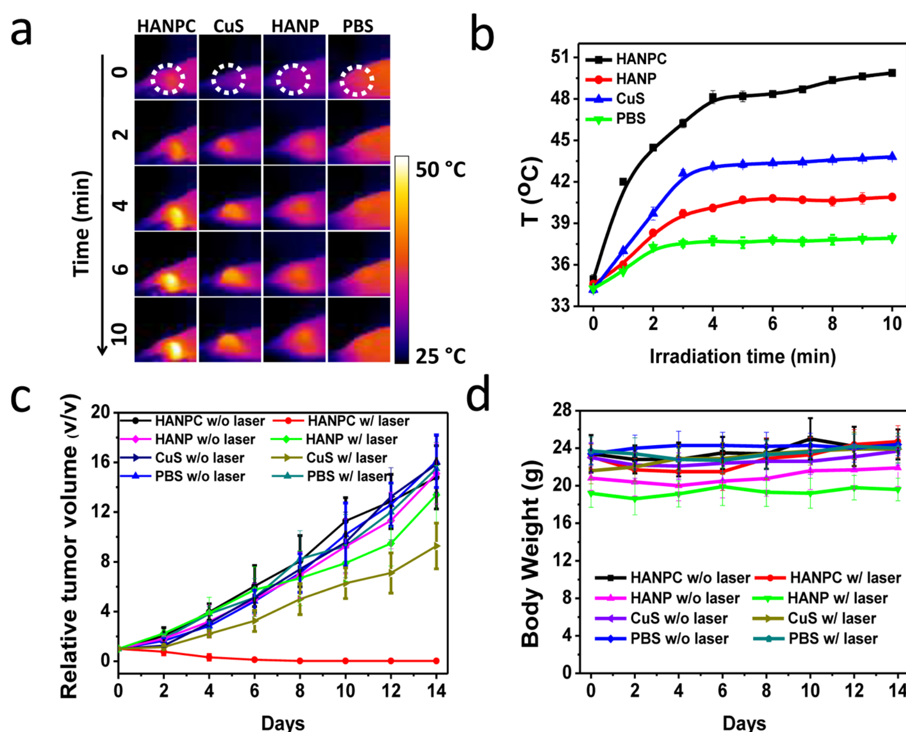

Figure 5. *In vivo* photothermal therapy (PTT). (a) Thermal images of SCC7 tumor-bearing mice iv treated with PBS, HANP, CuS, and HANPC (left row, 5 mg/kg of HANPC, illuminated at 6 h p.i.) with 808 nm laser illumination taken at indicated time points. The injected amount of HANP and CuS were calculated according to the loading efficiency. The laser power density was 1.5 W/cm^2. (b) Quantitative analysis of temperature changes in tumor area at different time points. (c) SCC7 tumor growth rate in each groups after indicated treatments. Tumor volumes were normalized to their initial size (n = 5 per group). For therapeutic groups, mice were intravenously received with HANPC and subjected to 808 nm laser irradiation (1.5 W/cm ^{2}, 10 min) at 6 h postinjection. Seven groups of mice were set as controls: PBS group with and without laser irradiation. free CuS group with and without laser irradiation. HANP group with and without laser irradiation. and HANPC group without laser irradiation. Error bars were based on standard error of mean (SEM). (d) Body weight curves of SCC7 tumor-bearing mice for each group.

was set as 1.5 W/cm^2 at 808 nm for 10 min. On the contrary, the PBS group only had a slight increase in temperature (33 to 37 °C) after 10 min irradiation (Figure 5a,b). Although a slight temperature increase was observed after HANP or CuS alone was injected at the same concentration as in the HANPC group along with laser irradiation, the temperature in the tumor area was not high enough to kill the cancer cells effectively. To verify the photothermal therapeutic effect of HANPC, we continued to monitor and record SCC7 tumor growth rates. The tumors on mice received HANPC treatment with laser irradiation demonstrated serious empyrosis resulting in ablation of tumor after NIR laser irradiation. In marked contrast, other control groups with laser irradiation at this power density or HANPC injected without laser irradiation did not show significant tumor suppression as shown in Figure 5c. These results suggested that PTT may have potential for cancers those are not deep in the tissue, for example breast cancer, skin tumors or cervical intraepithelial neoplasia. The development of special fiber optic probe instrument is required for translating PTT into clinic for deep primary tumor therapy in the future.

To further investigate HANPC-mediated PTT effect, we harvested the tumor tissues and main organs treated with PBS, HANP, CuS and HANPC with and without NIR irradiation. The tumors and organs were analyzed by H&E staining. Compared with control groups, the HANPC administrated group clearly showed tumor necrosis and destroyed blood vessels after laser irradiation treatment (Figure 6a), suggesting that HANPC effectively delivered CuS into the tumor tissue and induced tumor cell death with laser irradiation. No obvious destruction in tumor was found in either control groups or HANPC groups without laser irradiation. The major organs from SCC7 tumor-bearing nude mice of each group, including heart, liver, spleen, lung and kidney were analyzed. We did not observe any noticeable organ damage based on H&E stained organ slices (Figure 6b), showing that HANPC did not have toxic side effects in SCC7 tumor-bearing nude mice. Collectively, our results verified that HANPC was not toxic to mice and could serve as a promising optical/PA image-guided tumor PTT agent. The HANP particle could be an ideal platform for image guided therapy by loading different agents.

CONCLUSION

In summary, we successfully constructed an activatable nanocomplex, HANPC, for optical and photoacoustic image-guided PTT of SCC7 tumors. Due to the EPR effect and receptor-mediated endocytosis,

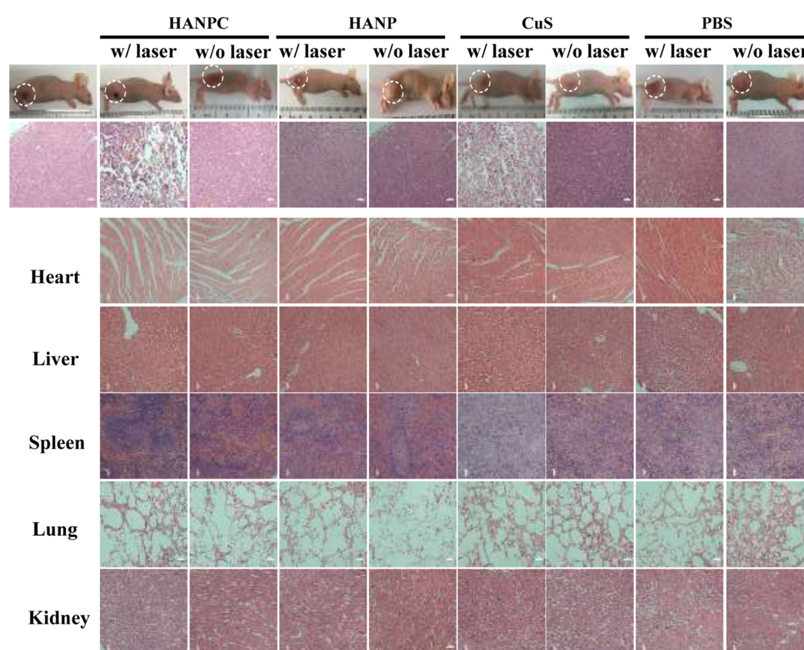

Figure 6. (a) Representative photos of mice after different treatments. H&E stained tumor sections collected from different groups of mice at indicated time points. Severely damaged tumor tissue was observed in HANPC treated group after irradiation. Arrows indicate the damages of blood vessels in the tumor. (b) H&E staining of major organs. No noticeable abnormality was found in the heart, liver, spleen, lung, or kidney.

HANPC demonstrated enhanced uptake in tumor tissue. The overexpressed hyaluronidase expression in tumor cells can efficiently degrade HANPC and therefore boost strong fluorescent signals to indicate tumor presence in the whole body. On the other hand, PA imaging is able to offer images with high resolution and sensitivity in the tumor area specifically. For example, PA imaging can monitor blood vessel distribution in the tumor region and the dynamic HANPC accumulation, which are very helpful for understanding the tumor microstructures and the intratumoral behaviors of targeting agents. After laser irradiation, tumors intravenously injected with HANPC were effectively ablated compared with control groups. Moreover, H&E staining suggest that no obvious cytotoxicity was observed in our study. Our results demonstrate that HANPC possess great potential for optical/PA image-guided therapy and the HANP system is expected to serve as a platform for other therapeutic agents, supporting simultaneous tumor diagnosis and treatment.

MATERIALS AND METHODS

Reagents. Sodium hyaluronic acid (HA, molecular weight = 2.34×10^2 kDa) was bought from Lifecore Biomedical company (Chaska, MN), and applied in our experiments after dialyzed against ultrapure water and lyophilized. Ethylenediamine (EDA), 1-ethyl-3(3-(dimethylamino)propyl)carbodiimide (EDC), and *N*-hydroxysuccinimide (NHS) were obtained from J&K company (Beijing, China). 5β-Cholanic acid (CA), tetrabutylammonium hydroxide (TBA) and propidium iodide (PI) were obtained from Sigma-Aldrich Co. (St. Louis, MO). Amine-PEG-amine (molecular weight = 2 kDa) was purchased from Shanghai Seebio Biotech (Shanghai, China). A NIR dye, Cy5.5-NHS, was obtained from GE Healthcare (Pittsburgh PA). Dulbecco's Modified Eagle Medium (DMEM) was obtained from Thermo Scientific (Beijing, China). Fetal bovine serum (FBS) and antibiotics were purchased from PAA (Chalfont St Giles, U.K.). Hyaluronidase, MTT assay kit and 4,6-diamidino-2-phenylindole (DAPI) were purchased form Bioengineering Co., Ltd. (Shanghai, China). Calcein-AM was obtained by Invitrogen (Grand Island NY). SCC7 (squamous cell carcinoma) and NIH-3T3 (mouse embryonic fibroblast cells) were bought from ATCC (Manassas, VA). Glass bottom cell culture dishes were obtained from NEST Biotechnology Co. LTD (Nanjing, China). Eppendorf tubes (1.5 mL), 6-well chambers, 96-well flat-bottomed plates and cell culture dishes were purchased from JET BIOFIL (Guangzhou, China). All the rest reagents were analytical grade and used with no other purifications.

Preparation and Characterization of HANPC. HANPC was prepared by High Pressure Homogenizer (PhD Technology International LLC, USA). In brief, hyaluronic acid (HA) was converted to the tetrabutylammonium salt of HA (HA-TBA) using a previously reported method,[38] so that it can be dissolved in DMSO. HA−5β-cholanic acid conjugation was synthesized by linking the carboxyl groups on HA-TBA with the amino groups on CA by EDC and NHS. Amine-PEG-amine was chemically conjugated to HA nanoparticles under the same conditions. Then, HA nanoparticles were labeled with Cy5.5-HNS dye in phosphate buffer (pH 7.8). Free Cy5.5 was removed by dialyzing Cy5.5 conjugated HA nanoparticles (HANP) in ultrapure water for 4 h. At last, HANP loaded CuS (HANPC) was readily prepared by mixing CuS dissolved in trichloromethane with HANP in ultrapure water and homogenized for 15−20 min (20 000−25 000 psi). The resulting mixture was added into the ultrafiltration tube (50 mL) and centrifuged at 4000 rpm and 4 °C for 10 min to remove free CuS, followed by freeze-drying.

CuS Loading Efficiency. First, CuS was dissolved in trichloromethane at concentrations of 0.2, 0.4, 0.6, and 0.8 mg/mL. A linear proportion was found between the concentration of CuS and its UV/vis/NIR absorbance with a regression equation of $Y = 0.304 + 2.155X$ ($R^2 = 0.9014$) (Supporting Information Figure S2b). Then,

the amount of CuS in HANPC at different loading contents was quantified using the standard curve (Table 1).

Cell Internalization of HANP. A total of 1×10^4 of SCC-7 and NIH-3T3 cells were, separately, seeded in a 6-well chamber at 37 °C overnight. On the second day, cells were washed by PBS and incubated with HANP (200 μg/mL) at 37 °C and 5% CO_2 atmosphere for 3 h. In another group, to verify the specificity of HA binding to CD44, free HA (2 mg/mL) was added to cells 30 min before HANP. After incubation, the cells were thoroughly washed three times with cold PBS. Then, cells were fixed in cold ethanol for 15 min at −20 °C. After the wash step with PBS, cells were mounted with mounting medium containing DAPI for 10 min in the dark. Cell uptake of HANP was observed by a confocal microscope (Leica, Germany), and the excitation and emission wavelengths were set at 670 and 690 nm for Cy5.5, respectively.

***In Vitro* Enzyme Activation of HANPC.** In the presence of the same concentration of hyaluronidase (Hyals), enzyme activation of HANPC was determined using a fluorescence imaging technique. In brief, HAase (2000 unit/well) was added into different concentrations (0−2 mg) of HANPC solutions in an acetate buffer (pH = 4.3) and incubated for 0, 30, 60, and 120 min at 37 °C. Fluorescent signals and images of HANPC solutions (0−2 mg/mL) were obtained at indicated time points using a fluorescence spectrophotometer (Varian, Palo Alto, CA) and Carestream FX PRO (Carestream Health Inc., Toronto, Canda).

***In Vitro* Photothermal Ablation Test.** To test the photothermal effect, HANP, HANPC, CuS and water solutions in 1.5 mL Eppendorf tubes were each irradiated with a NIR laser (808 nm, Stone laser, Shenzhen) at a power density of 1 W/cm^2 for 3 min. The laser spot covered the entire surface of samples. Thermal images of different solutions were acquired real-time by FLIR Ax5 camera (FLIR Systems Inc., Wilsonville, OR) and quantified by BM_IR software.

The SCC7 cells were cultured in DMEM/high glucose medium containing 10% FBS and 1% antibiotic solution at 37 °C and 5% CO_2. For MTT assay, SCC-7 cells at a density of 1×10^4 cells/well were seeded in a 96-well plate and cultured overnight. After a wash step with PBS, the cells were incubated with free CuS and HANPC solutions at different concentrations (5−1000 μg/mL, 100 μL/well) for 24 h at 37 °C and 5% CO_2. Experimental groups, which were replaced with fresh DMEM culture medium (100 μL), were irradiated with 808 nm laser for 10 min at a power density of 1 W/cm^2. The laser spot was adjusted to cover each well. Then, cells were incubated in 37 °C containing 5% CO_2 for 24 h. Cells in control groups were incubated under the same conditions without irradiation. Cell viability was evaluated by MTT assay.

Calcein AM/PI Staining. SCC7 cells were plated in glass bottom cell culture dishes with a density of 1×10^5 cell until grown to 80−90% confluency. After PBS washing, SCC7 cells were incubated with HANPC for 3 h. Next, SCC7 cells were washed with PBS for three times and immersed in 1 mL of fresh culture medium. Control groups without NIR laser irradiation were incubated in fresh DMEM medium at 37 °C. Experimental groups were illuminated with the laser beam (808 nm, 0.5 W/cm^2) for 10 min, followed by incubation for 2 h under identical conditions as the control groups. After removing fresh DMEM medium, SCC7 cells of all groups were added into Calcein AM (4 μmol/L) and PI solutions (4 μmol/L) in PBS and incubated for 30 min at 37 °C with 5% CO_2. Finally, cells were washed with PBS three times. Fluorescence images of cells were acquired by confocal microscopy.

***In Vivo* Imaging of SCC7 Tumor.** Animal experiments were conducted under protocols approved by Animal Care and Use Committee (CC/ACUCC) of Xiamen University. Subcutaneous sites of athymic nude mice (7 weeks old, female, 16−18 g) were injected a suspension of 4×10^6 SCC7 cells in PBS (80 μL). When tumor grow up to an average volume of 60−70 mm^3, 100 μL of HANP (5 mg/kg), CuS (174 μg), or HANPC (5 mg/kg containing 174 μg CuS) was intravenously injected, respectively. The fluorescent signals were observed using Carestream FX Pro and PA imaging in the tumor sites were recorded on Endra Nexus128 (Ann Arbor, MI) at 1, 2, 6, and 12 h time points, At 1, 6, and 12 h postinjection, tumors and normal organs including heart, liver, spleen, kidney, pancreas and muscle from SCC7 tumor-bearing nude mice were collected and visualized with Carestream FX Pro and Endra Nexus128.

***In Vivo* Photothermal Therapy of HANPC.** SCC-7 cells (4×10^6 cells per 80 μL of PBS) were injected in the right leg of nude mice (7 weeks old). When tumor size reached an average size of 60−70 mm^3, 100 μL of PBS, HANP (5 mg/kg), CuS (174 μg) and HANPC (5 mg/kg containing 174 μg CuS) was injected into the tail vein of the tumor-bearing mice, separetely. At 6 h post-injection, the tumors were illuminated with the 808 nm laser beam at a power density of 1.5 W/cm^2 for 10 min. Meanwhile, thermal images in tumors were taken with a FLIR Ax5 camera and quantified by BM_IR software.

The tumor-bearing mice were divided into eight groups randomly: (a) PBS without laser, (b) PBS with laser, (c) HANPC without laser, (d) HANPC with laser, (e) HANP without laser, (f) HANP with laser, (g) CuS without laser and (h) CuS with laser. When the tumor volume reached 60−70 mm^3 in size, 100 μL of PBS, HANP (5 mg/kg), CuS (174 μg) or HANPC (5 mg/kg containing 174 μg CuS) was injected intravenously, separately. After 6 h, the tumors in group of b, d, f, and h were irradiated by the 808 nm laser for 10 min at 1.5 W/cm^2. The mouse body weight was recorded. The following equation was used to monitor tumor growth (volume change): tumor volume = $A \times B^2/2$, where A is the largest and B is the smallest diameter.[39] Compared to the original tumor volume, the relative tumor volumes of all groups were calculated at 14 day after treatment. Hematoxylin and eosin (H&E) staining were applied for analyzing HANPC toxicity to tumor tissues and main organs.

Statistical Analysis. Experiment results were presented as mean ± SD. Statistical analysis was performed using one-way ANOVA followed by Bonferroni multiple comparison test. $P < 0.05$ was considered statistically significant.

Conflict of Interest: The authors declare no competing financial interest.

Acknowledgment. This work was supported by National High Technology Research and Development Program of China (863 Program) (No. 2014AA020708), National Science Foundation of China (NSFC) (81201129, 51373144 and 81271606).

Supporting Information Available: Chemical structures, UV/vis/NIR spectra, enzyme test, thermal images, biodistributions and photoacoustics signals of nanoparticles. This material is available free of charge *via* the Internet at http://pubs.acs.org.

REFERENCES AND NOTES

1. Guo, M.; Mao, H.; Li, Y.; Zhu, A.; He, H.; Yang, H.; Wang, Y.; Tian, X.; Ge, C.; Peng, Q.; *et al.* Dual Imaging-Guided Photothermal/Photodynamic Therapy Using Micelles. *Biomaterials* **2014**, *35*, 4656–4666.
2. Jing, L.; Liang, X.; Deng, Z.; Feng, S.; Li, X.; Huang, M.; Li, C.; Dai, Z. Prussian Blue Coated Gold Nanoparticles for Simultaneous Photoacoustic/Ct Bimodal Imaging and Photothermal Ablation of Cancer. *Biomaterials* **2014**, *35*, 5814–5821.
3. Lee, N.; Cho, H. R.; Oh, M. H.; Lee, S. H.; Kim, K.; Kim, B. H.; Shin, K.; Ahn, T. Y.; Choi, J. W.; Kim, Y. W.; *et al.* Multifunctional Fe3o4/Tao(X) Core/Shell Nanoparticles for Simultaneous Magnetic Resonance Imaging and X-Ray Computed Tomography. *J. Am. Chem. Soc.* **2012**, *134*, 10309–10312.
4. Topete, A.; Alatorre-Meda, M.; Iglesias, P.; Villar-Alvarez, E. M.; Barbosa, S.; Costoya, J. A.; Taboada, P.; Mosquera, V. Fluorescent Drug-Loaded, Polymeric-Based, Branched Gold Nanoshells for Localized Multimodal Therapy and Imaging of Tumoral Cells. *ACS Nano* **2014**, *8*, 2725–2738.
5. Wang, C.; Sun, X.; Cheng, L.; Yin, S.; Yang, G.; Li, Y.; Liu, Z. Multifunctional Theranostic Red Blood Cells for Magnetic-Field-Enhanced *in Vivo* Combination Therapy of Cancer. *Adv. Mater.* **2014**, *26*, 4794–4802.
6. Cheng, L.; Yang, K.; Chen, Q.; Liu, Z. Organic Stealth Nanoparticles for Highly Effective *in Vivo* near-Infrared Photothermal Therapy of Cancer. *ACS Nano* **2012**, *6*, 5605–5613.

7. Zhu, L.; Ma, Y.; Kiesewetter, D. O.; Wang, Y.; Lang, L.; Lee, S.; Niu, G.; Chen, X. Rational Design of Matrix Metalloproteinase-13 Activatable Probes for Enhanced Specificity. *ACS Chem. Biol.* **2014**, *9*, 510–516.
8. Zhu, L.; Huang, X.; Choi, K. Y.; Ma, Y.; Zhang, F.; Liu, G.; Lee, S.; Chen, X. Real-Time Monitoring of Caspase Cascade Activation in Living Cells. *J. Controlled Release* **2012**, *163*, 55–62.
9. Zhu, L.; Zhang, F.; Ma, Y.; Liu, G.; Kim, K.; Fang, X.; Lee, S.; Chen, X. *In Vivo* Optical Imaging of Membrane-Type Matrix Metalloproteinase (Mt-Mmp) Activity. *Mol. Pharmaceutics* **2011**, *8*, 2331–2338.
10. Zhu, L.; Xie, J.; Swierczewska, M.; Zhang, F.; Quan, Q.; Ma, Y.; Fang, X.; Kim, K.; Lee, S.; Chen, X. Real-Time Video Imaging of Protease Expression *in Vivo*. *Theranostics* **2011**, *1*, 18–27.
11. Ichikawa, Y.; Kamiya, M.; Obata, F.; Miura, M.; Terai, T.; Komatsu, T.; Ueno, T.; Hanaoka, K.; Nagano, T.; Urano, Y. Selective Ablation of Beta-Galactosidase-Expressing Cells with a Rationally Designed Activatable Photosensitizer. *Angew. Chem., Int. Ed.* **2014**, *53*, 6772–6775.
12. Chen, Q.; Wang, C.; Zhan, Z.; He, W.; Cheng, Z.; Li, Y.; Liu, Z. Near-Infrared Dye Bound Albumin with Separated Imaging and Therapy Wavelength Channels for Imaging-Guided Photothermal Therapy. *Biomaterials* **2014**, *35*, 8206–8214.
13. Yin, W.; Yan, L.; Yu, J.; Tian, G.; Zhou, L.; Zheng, X.; Zhang, X.; Yong, Y.; Li, J.; Gu, Z.; *et al.* High-Throughput Synthesis of Single-Layer Mos Nanosheets as a near-Infrared Photothermal-Triggered Drug Delivery for Effective Cancer Therapy. *ACS Nano* **2014**, *8*, 6922–6933.
14. Wu, X.; Sun, X.; Guo, Z.; Tang, J.; Shen, Y.; James, T. D.; Tian, H.; Zhu, W. *In Vivo* and *in Situ* Tracking Cancer Chemotherapy by Highly Photostable Nir Fluorescent Theranostic Prodrug. *J. Am. Chem. Soc.* **2014**, *136*, 3579–3588.
15. Choi, K. Y.; Min, K. H.; Na, J. H.; Choi, K.; Kim, K.; Park, J. H.; Kwon, I. C.; Jeong, S. Y. Self-Assembled Hyaluronic Acid Nanoparticles as a Potential Drug Carrier for Cancer Therapy: Synthesis, Characterization, and *in Vivo* Biodistribution. *J. Mater. Chem.* **2009**, *19*, 4102.
16. Choi, K. Y.; Chung, H.; Min, K. H.; Yoon, H. Y.; Kim, K.; Park, J. H.; Kwon, I. C.; Jeong, S. Y. Self-Assembled Hyaluronic Acid Nanoparticles for Active Tumor Targeting. *Biomaterials* **2010**, *31*, 106–114.
17. Choi, K. Y.; Min, K. H.; Yoon, H. Y.; Kim, K.; Park, J. H.; Kwon, I. C.; Choi, K.; Jeong, S. Y. Pegylation of Hyaluronic Acid Nanoparticles Improves Tumor Targetability *in Vivo*. *Biomaterials* **2011**, *32*, 1880–1889.
18. Park, J. H.; Cho, H. J.; Yoon, H. Y.; Yoon, I. S.; Ko, S. H.; Shim, J. S.; Cho, J. H.; Park, J. H.; Kim, K.; Kwon, I. C.; *et al.* Hyaluronic Acid Derivative-Coated Nanohybrid Liposomes for Cancer Imaging and Drug Delivery. *J. Controlled Release* **2014**, *174*, 98–108.
19. Schledzewski, K.; Falkowski, M.; Moldenhauer, G.; Metharom, P.; Kzhyshkowska, J.; Ganss, R.; Demory, A.; Falkowska-Hansen, B.; Kurzen, H.; Ugurel, S.; *et al.* Lymphatic Endothelium-Specific Hyaluronan Receptor Lyve-1 Is Expressed by Stabilin-1+, F4/80+, Cd11b+ Macrophages in Malignant Tumours and Wound Healing Tissue *in Vivo* and in Bone Marrow Cultures *in Vitro*: Implications for the Assessment of Lymphangiogenesis. *J. Pathol.* **2006**, *209*, 67–77.
20. Lapcik, L., Jr.; Lapcik, L.; De Smedt, S.; Demeester, J.; Chabrecek, P. Hyaluronan: Preparation, Structure, Properties, and Applications. *Chem. Rev.* **1998**, *98*, 2663–2684.
21. Stern, R. Hyaluronidases in Cancer Biology. *Semin Cancer Biol.* **2008**, *18*, 275–280.
22. Itano, N. Simple Primary Structure, Complex Turnover Regulation and Multiple Roles of Hyaluronan. *J. Biochem.* **2008**, *144*, 131–137.
23. Zha, Z.; Yue, X.; Ren, Q.; Dai, Z. Uniform Polypyrrole Nanoparticles with High Photothermal Conversion Efficiency for Photothermal Ablation of Cancer Cells. *Adv. Mater.* **2013**, *25*, 777–782.
24. Wan, Z.; Mao, H.; Guo, M.; Li, Y.; Zhu, A.; Yang, H.; He, H.; Shen, J.; Zhou, L.; Jiang, Z.; *et al.* Highly Efficient Hierarchical Micelles Integrating Photothermal Therapy and Singlet Oxygen-Synergized Chemotherapy for Cancer Eradication. *Theranostics* **2014**, *4*, 399–411.
25. Jin, Y.; Li, Y.; Ma, X.; Zha, Z.; Shi, L.; Tian, J.; Dai, Z. Encapsulating Tantalum Oxide into Polypyrrole Nanoparticles for X-Ray Ct/Photoacoustic Bimodal Imaging-Guided Photothermal Ablation of Cancer. *Biomaterials* **2014**, *35*, 5795–5804.
26. Bai, J.; Liu, Y.; Jiang, X. Multifunctional Peg-Go/Cus Nanocomposites for near-Infrared Chemo-Photothermal Therapy. *Biomaterials* **2014**, *35*, 5805–5813.
27. Fiedler, V. U.; Schwarzmaier, H. J.; Eickmeyer, F.; Muller, F. P.; Schoepp, C.; Verreet, P. R. Laser-Induced Interstitial Thermotherapy of Liver Metastases in an Interventional 0.5 T Mri System: Technique and First Clinical Experiences. *J. Magn. Reson. Imaging* **2001**, *13*, 729–737.
28. Yang, K.; Feng, L.; Shi, X.; Liu, Z. Nano-Graphene in Biomedicine: Theranostic Applications. *Chem. Soc. Rev.* **2013**, *42*, 530–547.
29. Zha, Z.; Zhang, S.; Deng, Z.; Li, Y.; Li, C.; Dai, Z. Enzyme-Responsive Copper Sulphide Nanoparticles for Combined Photoacoustic Imaging, Tumor-Selective Chemotherapy and Photothermal Therapy. *Chem. Commun.* **2013**, *49*, 3455–3457.
30. Li, Y.; Lu, W.; Huang, Q.; Huang, M.; Li, C.; Chen, W. Copper Sulfide Nanoparticles for Photothermal Ablation of Tumor Cells. *Nanomedicine (London, U.K.)* **2010**, *5*, 1161–1171.
31. Tian, Q.; Jiang, F.; Zou, R.; Liu, Q.; Chen, Z.; Zhu, M.; Yang, S.; Wang, J.; Wang, J.; Hu, J. Hydrophilic Cu9s5 Nanocrystals: A Photothermal Agent with a 25.7% Heat Conversion Efficiency for Photothermal Ablation of Cancer Cells *in Vivo*. *ACS Nano* **2011**, *5*, 9761–9771.
32. Ku, G.; Zhou, M.; Song, S.; Huang, Q.; Hazle, J.; Li, C. Copper Sulfide Nanoparticles as a New Class of Photoacoustic Contrast Agent for Deep Tissue Imaging at 1064 Nm. *ACS Nano* **2012**, *6*, 7489–7496.
33. Yang, K.; Zhu, L.; Nie, L.; Sun, X.; Cheng, L.; Wu, C.; Niu, G.; Chen, X.; Liu, Z. Visualization of Protease Activity *in Vivo* Using an Activatable Photo-Acoustic Imaging Probe Based on Cus Nanoparticles. *Theranostics* **2014**, *4*, 134–141.
34. Ramadan, S.; Guo, L.; Li, Y.; Yan, B.; Lu, W. Hollow Copper Sulfide Nanoparticle-Mediated Transdermal Drug Delivery. *Small* **2012**, *8*, 3143–3150.
35. Ding, C.; Zhong, H.; Zhang, S. Ultrasensitive Flow Injection Chemiluminescence Detection of DNA Hybridization Using Nanocus Tags. *Biosens. Bioelectron.* **2008**, *23*, 1314–1318.
36. Zhou, M.; Zhang, R.; Huang, M.; Lu, W.; Song, S.; Melancon, M. P.; Tian, M.; Liang, Dong; Li, C. A Chelator-Free Multifunctional [64cu]Cus Nanoparticle Platform for Simultaneous Micro-Pet/Ct Imaging and Photothermal Ablation Therapy. *J. Am. Chem. Soc.* **2010**, *132*, 15351–15358.
37. Tian, Q.; Tang, M.; Sun, Y.; Zou, R.; Chen, Z.; Zhu, M.; Yang, S.; Wang, J.; Wang, J.; Hu, J. Hydrophilic Flower-Like Cus Superstructures as an Efficient 980 nm Laser-Driven Photothermal Agent for Ablation of Cancer Cells. *Adv. Mater.* **2011**, *23*, 3542–3547.
38. Oh, E. J.; Kim, J. W.; Kong, J. H.; Ryu, S. H.; Hahn, S. K. Signal Transduction of Hyaluronic Acid-Peptide Conjugate for Formyl Peptide Receptor Like 1 Receptor. *Bioconjugate Chem.* **2008**, *19*, 2401–2408.
39. Hoeck, J. D.; Jandke, A.; Blake, S. M.; Nye, E.; Spencer-Dene, B.; Brandner, S.; Behrens, A. Fbw7 Controls Neural Stem Cell Differentiation and Progenitor Apoptosis *Via* Notch and C-Jun. *Nat. Neurosci.* **2010**, *13*, 1365–1372.